JACS
JOURNAL OF THE AMERICAN CHEMICAL SOCIETY

ARTICLE

pubs.acs.org/JACS

Stepwise Neutral−Ionic Phase Transitions in a Covalently Bonded Donor/Acceptor Chain Compound

Hitoshi Miyasaka,*[,†] Natsuko Motokawa,[†] Tamiko Chiyo,[†] Miho Takemura,[†] Masahiro Yamashita,[†] Hajime Sagayama,[‡] and Taka-hisa Arima[‡]

[†]Department of Chemistry, Graduate School of Science, Tohoku University, 6-3 Aramaki-Aza-Aoba, Sendai 980-8578, Japan

[‡]Institute of Multidisciplinary Research for Advanced Materials, Tohoku University, Sendai 980-8577, Japan

Supporting Information

ABSTRACT: Neutral (N)−ionic (I) transitions in organic donor (D)/acceptor (A) charge-transfer complexes are intriguing because a 'reservoir of functions' is available. For systematically controlling N−I transitions, tuning the ionization potential of D and the electron affinity of A is extremely important. However, the effect of Coulomb interactions, which likely causes a number of charge-gap states at once in a system bringing about stepwise transitions, is a long-standing mystery. Here, we show definite evidence for stepwise N−I transitions caused by contributions from anisotropic interchain Coulomb interactions in a metal-complex-based covalently bonded DA chain compound, $[Ru_2(2,3,5,6\text{-}F_4PhCO_2)_4(DMDCNQI)]\cdot 2(p\text{-xylene})$ (**1**; $2,3,5,6\text{-}F_4PhCO_2^-$ = 2,3,5,6-tetrafluorobenzoate; DMDCNQI = 2,5-dimethyl-*N*,*N*′-dicyanoquinonediimine), where the $[Ru_2^{II,II}(2,3,5,6\text{-}F_4PhCO_2)_4]$ moiety has a paddlewheel diruthenium(II,II) motif with a Ru−Ru bond. An intermediate-temperature phase involving self-organized N and *I* chains was observed in the temperature range between 210 K (= T_2) and 270 K (= T_1) with N phase at $T > T_1$ and I phase at $T < T_2$. Accompanying the charge transitions, the spin−ground states as well as the ferrimagnetic ordering in the I phase vary. The stepwise feature of the N−I transition with a highly sensitive magnetic response should bring about new dynamical functionalities associated with charge, spin, and lattice.

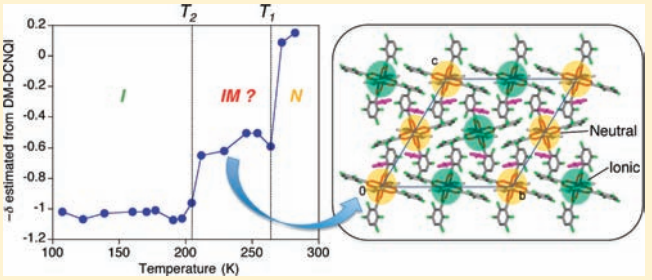

INTRODUCTION

Comprehensive studies on the control and quantification of charge transfer between electron donors (D) and acceptors (A) have been most successful using cocrystallized organic π-DA molecules.[1,2] Fine tuning of the ionization potential (I_D) of D and the electron affinity (E_A) of A in 1:1 $D^{\delta+}A^{\delta-}$ complexes (δ: the degree of charge transfer) can be used to control phase transitions between distinct valence states of the neutral (N: D^0A^0 with $\delta = 0$) and ionic (I: D^+A^- with $\delta = 1$) states, i.e., the so-called N−I phase transition, which is triggered by external modulations, such as temperature,[3,4] pressure,[5−12] and photoirradiation.[13−17] A tetrathiafulvalene/*p*-chloranil compound (TTF-CA) was the first reported example of compound exhibiting an N−I phase transition.[3,4] Accompanying this 'switch of charge,' several fundamental physical properties, such as emergent electron transport caused by charge fluctuations,[3,4] magnetism,[18] and dielectric properties induced by structural modifications,[19−23] are reversibly modified, making it possible to prepare multiple switchable materials controlled by applying magnetic[23] and electric fields.[24,25] Although there has been a large amount of interest in systems exhibiting N−I transitions, examples are still limited to materials comprised of 'stacked' π-DA systems of organic compounds.[4,8,12,21,26−31] Most of these systems therefore exhibit a one-step N−I transition involving lattice dimerization in the I phase to form spin-singlet pairs.[32,33]

In order to systematically control N−I transitions, tuning I_D of D and E_A of A is the most important.[4] Meanwhile, the effect of Coulomb interactions, which can cause the formation of a number of charge-gap states at once allowing stepwise transitions to occur even in homogeneous DA systems, has been a long-standing mystery since Hubbard and Torrance[34] and Bak et al.[35,36] theoretically predicted such a stepwise feature 30 years ago, where they hence called it 'devil's staircase'. Although a two-step N−I transition upon application of pressure to a stacked assembly of 3,3′,5,5′-tetramethybenzidine/7,7,8,8-tetracyanoquinodimethane (TCNQ) has been reported, crucial information about the intermediate phase has not yet been reported.[11] Here, we report temperature-induced two-stage N−I phase transitions in a covalently bonded DA chain compound due to contributions from anisotropic interchain Coulomb interactions. The present covalently bonded DA chain compound is $[Ru_2(2,3,5,6\text{-}F_4PhCO_2)_4(DMDCNQI)]\cdot 2(p\text{-xylene})$ (**1**; $2,3,5,6\text{-}F_4PhCO_2^-$ = 2,3,5,6-tetrafluorobenzoate; DMDCNQI = 2,5-dimethyl-*N*,*N*′-dicyanoquinonediimine), where the $[Ru_2^{II,II}(2,3,5,6\text{-}F_4PhCO_2)_4]$ moiety has a paddlewheel diruthenium(II,II) motif with a Ru−Ru bond (hereafter abbreviated as $[Ru_2^{II,II}]$). Accompanying stepwise

Received: November 8, 2010
Published: March 16, 2011

   dx.doi.org/10.1021/ja110007u | *J. Am. Chem. Soc.* 2011, 133, 5338–5345

Chart 1. Schematic Representations of (a) Paddlewheel Diruthenium Units and the Quinonoid and (b) Benzenoid Forms of DMDCNQI with the Assignment of Respective Bonds *a*−*f* for Figure 2b

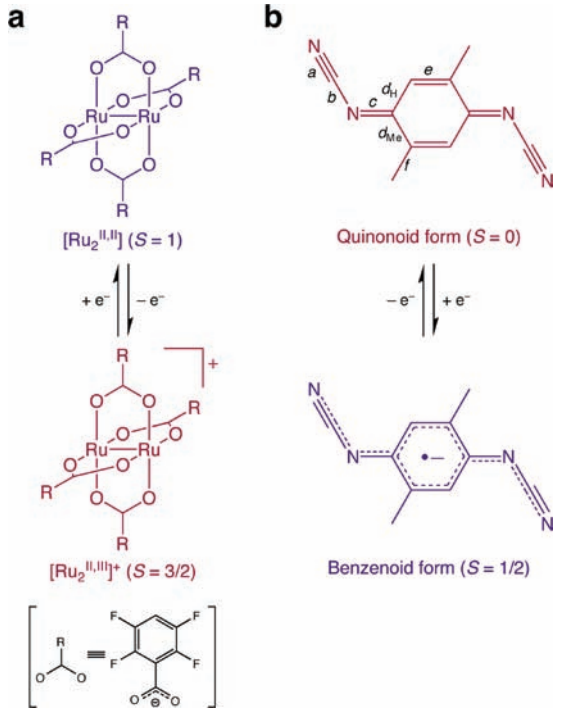

charge transitions, δ for $D^{\delta+}A^{\delta-}$ varies reversibly between 0 and ~0.5 at T_1 and then 0.5 and 1 at T_2 ($<T_1$). In addition to precise characterization of the two phases and the intermediate (IM) phase with a formal charge of $\delta = 0.5$, highly sensitive magnetic and electronic responses accompanying the N−I transitions were evaluated.

RESULTS AND DISCUSSION

Compound **1** is composed of an array of chains of alternating covalently bonded carboxylate-bridged paddlewheel diruthenium(II,II) complexes, $[Ru_2^{II,II}(2,3,5,6\text{-}F_4PhCO_2)_4]$, and DMDCNQI units. $[Ru_2^{II,II}]$ with $S = 1$[37,38] can act as a donor forming $[Ru_2^{II,III}]^+$ with $S = 3/2$[39] (as D^+) without any significant structural changes (Chart 1a),[40] and DCNQI is a well-known π-acceptor,[41] which becomes a radical anion ($DCNQI^{\bullet-}$, denoted as A^-) with $S = 1/2$ (Chart 1b).[42,43] Even in such covalently bonded DA assemblies, tuning I_D of D and E_A of A is important for systematically controlling the oxidation state, as shown in D_2A assembled systems composed of $[Ru_2]$ and TCNQ derivatives.[44−49] In fact, the presence of the fluoro groups, which have electron-withdrawing character, at the 2, 3, 5, and 6 positions of the benzoate ligands of $[Ru_2^{II,II}]$[50] and use of DMDCNQI resulted in the formation of the neutral chain **1** at room temperature.

From single-crystal X-ray analysis using a commercial CCD X-ray diffractometer in the temperature range of 107−282 K, the complex has a one-dimensional (1-D) chain motif with a [−{Ru_2}−(DMDCNQI)−] repeat (Figure 1a) in the monoclinic $P2_1/n$ with $Z = 2$. No distinct diffraction spots indicating a lower symmetry structure were observed under the measurement conditions. These data will be used hereafter to discuss averaged structures, even that of the IM phase, whereas data obtained from

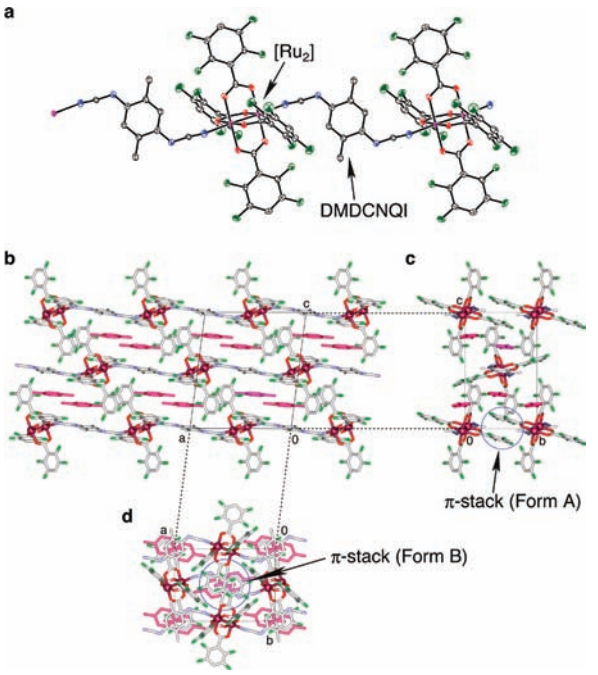

Figure 1. Chain structure of **1** at 107 K (a) composed of $[Ru_2(2,3,5,6\text{-}F_3PhCO_2)_4]$ and DMDCNQI subunits (50% probability ellipsoids; hydrogen atoms were omitted for clarity) and packing diagrams projected along the *b* (b), *a* (c), and *c* axes (d), respectively (C, white; F, green; N, blue; O, red; Ru, purple for the chain, and *p*-xylene was colored in pink; hydrogen atoms were omitted for clarity). In (c) and (d), blue circles indicate π stack forms (Form A and B; see text).

synchrotron X-ray diffraction analyses will be used to discuss the true structure (vide infra). The chains run along the *a* axis of the unit cell (Figure 1b) and are arranged in anisotropic π stacks along the *b* axis with repeating $[Ru_2]$ units and slipped π stacks in parts of the 2,3,5,6-F_4Ph groups (Form A; Figure 1c) and along the *c* axis in a $[\cdots(DMDCNQI)^{\alpha}\cdots(p\text{-xylene})\cdots(F_4Ph)^{\beta}\cdots(F_4Ph)^{\gamma}\cdots(p\text{-xylene})\cdots]$ arrangement (Form B, which includes Form A in the $\cdots(F_4Ph)^{\beta}\cdots(F_4Ph)^{\gamma}\cdots$ part; Figure 1d), where F_4Ph is the 2,3,5,6-F_4Ph group of $[Ru_2]$ and the superscripts $\alpha-\gamma$ distinguish respective moieties coming from different adjacent chains. The mean-plane distances in the π stack forms are in the range of 2.93−3.45 Å (at 107 K). Chains align in-phase along the *b* axis with a distance of 10.519(3) Å between $[Ru_2]$ units and antiphase in the ⟨011⟩ direction with a distance of 10.0603(3) Å between $[Ru_2]$ and DMDCNQI (at 107 K). Thus, the chains align in-phase along the *b* axis and antiphase in the ⟨011⟩ direction. This anisotropic chain arrangement has important implications for understanding the features of stepwise phase transitions.

The Ru−O_{eq} length (O_{eq} = equatorial oxygen atoms) is quite sensitive to the oxidation state of the $[Ru_2]$ subunit: 2.06−2.07 Å for $[Ru_2^{II,II}]$ and 2.02−2.03 Å for $[Ru_2^{II,III}]^+$.[39] The average Ru−O_{eq} bond length (Table S1, Supporting Information) is plotted as a function of temperature in Figure 2a. At 282 K, the Ru−O_{eq} bond length was in the range of 2.06−2.07 Å, indicating an oxidation state of $[Ru_2^{II,II}]$. Upon cooling, it suddenly decreased to around 2.04−2.05 Å at ~270 K (T_1) and decreased to the range of 2.02−2.03 Å at ~210 K (T_2). Below T_2, the oxidation state of the $[Ru_2]$ unit is close to $[Ru_2^{II,III}]^+$. In between T_1 and T_2, the oxidation state is between both oxidation states, namely $[Ru_2]^{\delta+}$ where δ is formally ~0.5 (IM phase). In addition, the axial bond

dx.doi.org/10.1021/ja110007u |*J. Am. Chem. Soc.* 2011, 133, 5338–5345

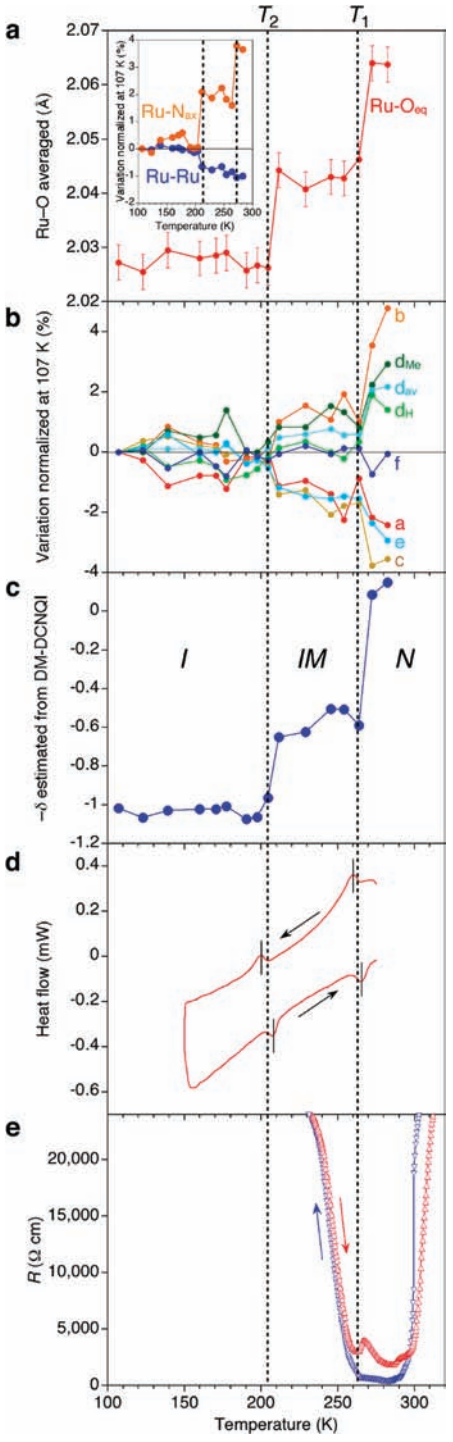

Figure 2. Structural variations and electrical resistivity as a function of temperature (for a−c, all structures were determined using the monoclinic space group $P2_1/n$). (a) Variation in the averaged Ru−O_{eq} bond (O_{eq} = carboxylate oxygen atoms) normalized to the value at 107 K, where the inset is the variations in the Ru−Ru and Ru−N_{ax} bonds (N_{ax} = cyanide nitrogen atom of DMDCNQI). (b) Variations in the local bonds of the DMDCNQI subunit normalized to the values at 107 K, where *a*−*f* are defined in Chart 1b and d_{av} stands for the average value between d_H and d_{Me}. (c) The degree of charge $-\delta$ on the DMDCNQI subunit estimated by using the Kistenmacher relationship. (d) Temperature dependence of the heat flow obtained from DSC (sweep rate, 5 °C/min). (e) Temperature dependence of electrical resistivity *R* measured on a single crystal along the *a* axis (two-probe method).

length (Ru−N_{ax}), which is also sensitive to the oxidation state of the [Ru_2] unit, became shorter at T_1 and T_2 with cooling down (Table S1, Supporting Information, and inset of Figure 2a).

Neutral DMDCNQI has a quinonoid structure (top of Chart 1b) with characteristic single (*b* and *d* in Chart 1b), double (C═C; *c* and *e*) and triple (C≡N; *a*) bonds, whereas anionic DMDCNQI (i.e., $DMDCNQI^{\bullet-}$) has a nearly benzenoid structure (bottom of Chart 1b) with an unpaired electron delocalized over the entire complex, causing an averaging of the bond lengths. As shown in Figure 2b, *a*, *c*, and *e* became longer at T_1 and T_2 in stepwise manner upon cooling in the range of 282−107 K, whereas *b* and *d* became shorter. Bond *f*, which is not involved in the resonance scheme, did not change in the temperature range. On the $DMDCNQI^{\delta-}$ moiety, δ was estimated by using the Kistenmacher relationship[51] $\delta = -\{A_\rho[c/(b+d)] + B_\rho\}$ in relation to the neutral chain [$Rh_2^{II,II}(CF_3CO_2)_4$(DMDCNQI)] ($\delta = 0$)[52] and the ionic chain [Mn^{III}(TMesP)(DMDCNQI)] (TMesP = *meso*-tetrakis(2,4,6-trimethylphenyl)porphyrinate; $\delta = 1$)[53] with $A_\rho = -36.900$ and $B_\rho = 17.295$. From a plot of the estimated values (Table S2, Supporting Information) versus *T* (Figure 2c), the DMDCNQI moiety has a quinonoid structure at around room temperature. In other words, the chain is neutral (N form) when $T > T_1$. Then DMDCNQI converts to a quasi-benzenoid form, meaning the chain becomes ionic (I form) with $\delta \approx 1$, when $T < T_2$. The IM form is a 'stage of charge' with a formal δ of ~0.5 between T_1 and T_2. The change in DMDCNQI is consistent with the change in the oxidation state of the [Ru_2] subunit, showing structurally that stepwise N−I phase transitions occur at T_1 and T_2. We confirmed by using differential scanning calorimetry (DSC) that these first-order transitions were reversible exo/endothermal processes with a small hysteresis in the cooling and heating processes, respectively (Figure 2d).

In order to elucidate the structure of the IM phase, X-ray diffraction measurements on a single crystal using a synchrotron beam were performed while heating. Figure 3a shows X-ray oscillation photographs of the I (200 K) and IM (220 K) phases. Superlattice reflections with a modulation vector (0 1/2 1/2) were clearly observed at 220 K. The typical intensity of the superlattice spots was weaker by 3 orders of magnitude than the fundamental reflections. The temperature dependence of the intensity of a superlattice reflection (−7 2.5 −0.5), shown in Figure 3b, indicates that a superlattice is present only in the IM phase. Moreover, some high-angle Bragg spots are split in the IM phase as shown in Figure 3c, indicating that the [011] and [0−11] axes are not equivalent. Both the 2_1 screw and glide operations break down, and hence the crystal symmetry is lowered to triclinic. The detailed analysis, which was performed taking account of the twinning, showed that the lengths of the [01−1] and [001] axes in the triclinic IM phase, corresponding the [011] and [0−11] axes in the monoclinic setting, respectively, are 20.42 and 20.45 Å. The simultaneous breaking of these symmetries is well in accord with the first-order nature of the transitions at T_1 and T_2. The appearance of the superlattice and the unchanged periodicity along the chain, i.e., along the *a* axis, in the IM phase strongly implies a regular arrangement of nonequivalent chains in the crystal. The superlattice unit cell of the IM phase based on the triclinic space group $P\bar{1}$ contains four structurally independent chains (I−IV), as shown in the middle panel of Figure 4b. The Ru−O_{eq} and bond lengths *a*−*f* in DMDCNQI for each chain were determined using structural parameters obtained at 240 K (Tables S3 and S4, Supporting Information). The extent of charge transfer for chains I−IV was

dx.doi.org/10.1021/ja110007u |*J. Am. Chem. Soc.* 2011, 133, 5338–5345

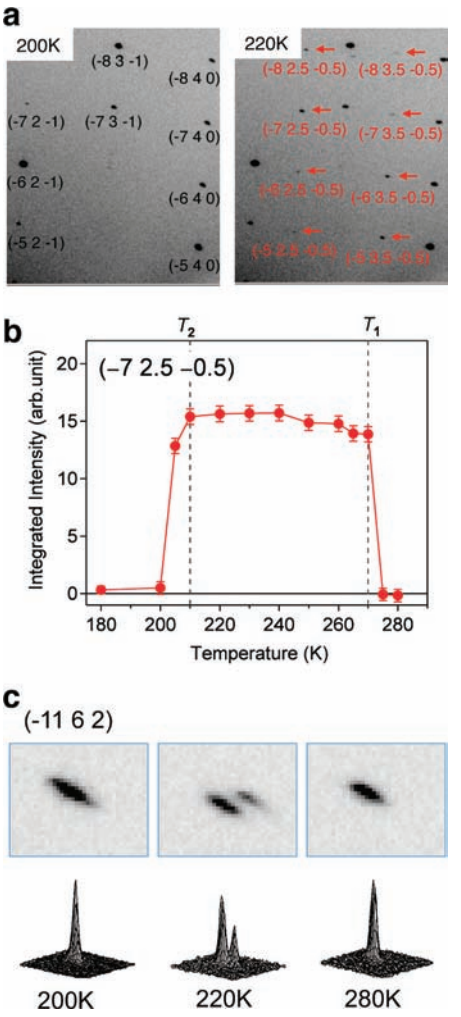

Figure 3. X-ray superlattice reflections in the intermediate (IM) phase. (a) Synchrotron X-ray oscillation photographs recorded at 200 K ($T < T_2$; left) and 220 K ($T_2 < T < T_1$; right). A series of $(h, k + 1/2, l + 1/2)$ reflections are discernible at 220 K. (b) Temperature dependence of the integrated intensity of the superlattice reflection $(-7\ 2.5\ -0.5)$. (c) Split of $(-11\ 6\ 2)$ reflection in the IM phase.

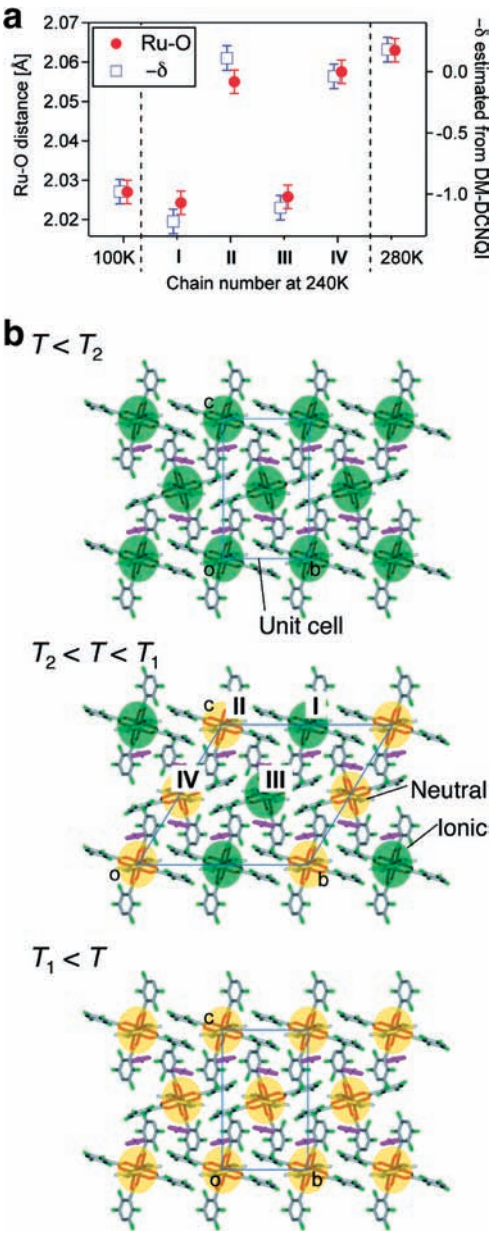

Figure 4. Arrangement of neutral (N) and ionic (I) chains in the intermediate (IM) phase. (a) The Ru−O_{eq} bond lengths (red solid circles) and degree of charge $-\delta$ on the DMDCNQI subunit estimated by using the Kistenmacher relationship (blue open squares) on each chain at 240 K (IM phase) deduced from the present synchrotron X-ray measurement. Four chains in a superlattice unit cell in the IM phase are labeled as shown in the middle panel of (b). Chains I and III are regarded as ionic, whereas II and IV are neutral. (b) Arrangements of N and I chains in the I phase below T_2 (top), IM phase between T_1 and T_2 (middle), and N phase above T_1 (bottom) projected onto the *bc* plane. Yellow and green denote the N and I chains, respectively.

estimated to be 1.22(13), −0.11(13), 1.11(14), and 0.04(13), respectively, by using the Kistenmacher relationship (Figure 4a). The Ru−O_{eq} bond lengths in II/IV are considerably longer than those in I/III (Table S3, Supporting Information and Figure 4a); this trend agrees with the assignment of $[Ru_2^{II,II}]$ and $[Ru_2^{II,III}]^+$ for II/IV and I/III, respectively, while those in II/IV are a little shorter than in the high-temperature N phase. These results suggest that two kinds of N chains (II and IV) with $\delta \approx 0$ and other two kinds of I chains (I and III) with $\delta \approx 1$ are aligned to form an alternating stack of N and I layers, as shown in Figure 4b. This is the first observation of self-organized N and I chains in an IM phase causing a stage for stepwise transitions.

The 1:1 alignment of N and I chains can be explained by taking into account electrostatic Coulomb interactions. As already mentioned, two neighboring chains are aligned in-phase along the *b* axis. A Coulomb energy cost is necessary for two chains to change simultaneously from N to I states. For this reason, having two I chains along the *c* axis is an unstable configuration. On the other hand, the next neighbor chains in the ⟨011⟩ direction are aligned antiphase. In this case, two chains can become I chains with a Coulomb energy gain. The Coulomb interactions prevent a uniform N−I transition and instead give rise to a complicated arrangement of N and I chains, as shown in Figure 4b. Below T_2, the intrachain energy gain of the I state becomes large enough to overcome the Coulomb energy cost, allowing a uniform I state to form.

The 1:1 mixture of N and I chains in the IM phase was confirmed by using infrared absorption spectroscopy on a single crystal. Characteristic C═C stretching modes ($\nu_{C=C}$) of DMDCNQI

dx.doi.org/10.1021/ja110007u |*J. Am. Chem. Soc.* 2011, 133, 5338–5345

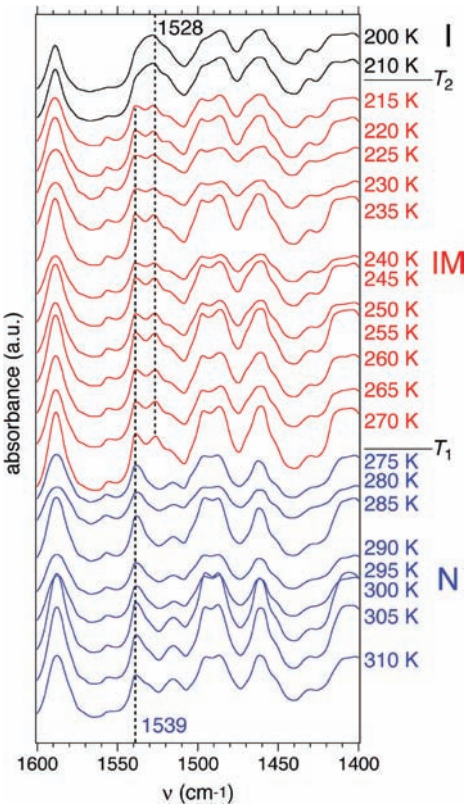

Figure 5. Infrared absorption spectra of **1** in the wavenumber range of 1400−1600 cm^{-1} measured on a single crystal, where the bands at 1539 and 1528 cm^{-1} correspond to ν(C═C) of the neutral and ionic DMDCNQI moieties, respectively (blue, red, and black lines represent ones for N, IM, and I phases, respectively).

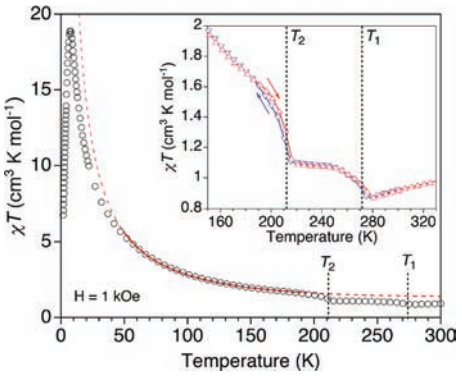

Figure 6. Temperature dependence of χT of **1** (cooling process), where the solid red line was fitted for the temperature range of 50−190 K using an alternating model of $S_i = 3/2$ and $S_{i+1} = 1/2$ (see text). The inset is a close-up view of the T range of 150−330 K (blue plot, cooling process; red plot, heating process).

were observed in the frequency range of 1400−1600 cm^{-1} (Figure 5; heating process). In the T range of 275−310 K, $\nu_{C=C}$ was observed as a single band at 1539 cm^{-1}, corresponding to the N state of DMDCNQI (e.g., 1537 cm^{-1} for free DMDCNQI^0). However, in the T range of 270−215 K, another band at 1528 cm^{-1}, assigned to $\nu_{C=C}$ for the I state, appeared without the loss or shifting of the band for the N state and then below 210 K, only the band for the I state remained. These changes took place at ∼270 and ∼210 K, which correspond to T_1 and T_2, respectively. Importantly, the characteristic bands for the N and I states coexist in the range of 270−215 K, i.e., the IM phase, without any new band that indicates the presence of a uniform $D^{0.5+}A^{0.5-}$ state in each chain. A similar trend was observed in the C≡N stretching modes ($\nu_{C\equiv N}$) (Figure S1, Supporting Information). These results agree with the synchrotron X-ray structural study.

N−I transitions are accompanied by drastic variations in the electron-transport properties. Figure 2e shows the temperature dependence of the electrical resistivity of a single crystal sample measured using a two-probe dc method along the a axis, i.e., chain direction. The resistivity was over 3.0×10^4 Ω cm when $T > 310$ K (almost insulator). However, upon cooling, it suddenly decreased to 4.0×10^2 Ω cm at 284 K and then increased again with an inflection at 263 K. The inflection also occurs in the heating process, although it makes a small peak at 266 K. On the basis of the magnitude of the resistivity, **1** can be regarded as a semiconductor over the entire temperature range. Therefore, such a decrease in the resistivity is unusual and is due to the N−I phase transition at T_1. In the TTF-CA system, the emergent conductance occurring just prior to the N−I phase transition was concluded to be due to the transport of charged and/or spin solitons in the dimerized I phase or the N−I domain walls.[6,18,54] A similar feature was observed in a D_2A-type two-electron transferred $[Ru_2]_2TCNQ$ system, in which thermally induced charge fluctuation between $D^{\delta+}$ and $A^{\delta-}$ is the cause.[49] Because no dimerization occurs along the chain, the anomalous decrease in resistivity at around T_1 was ascribed to charge fluctuations. One might think that δ would fluctuate in the IM phase where N and I chains coexist. However, Coulomb interactions between N and I chains and the resultant long-range ordering of the N and I chains prevent δ from fluctuating. The charge fluctuation is thus enhanced just above the temperature where long-range ordering appears; so, the increase in the resistivity occurs abruptly around T_1.

The change in the magnetic state accompanying the N−I phase transition is one of the most important features of this system because the variety of utilizable spins and their strong magnetic correlations even at low magnetic fields confer an advantage on such a covalently bonded system based on transition-metal complexes. This is in sharp contrast to the case of mixed stack organic systems, where the antiferromagnetic interactions between neighboring quantum spins often causes dimerization to form spin-singlet pairs. In the present system, a new strongly coupled spin set is generated in the I state ($S = 3/2$ for $[Ru_2^{II,III}]^+$ and $S = 1/2$ for $DMDCNQI^{\bullet-}$) from the paramagnetic N state with a sole contribution from the $[Ru_2^{II,II}]$ species with $S = 1$. It should be noted here that no structural evidence for dimerization was found, possibly due to the covalent bonding in the chains. In accordance with the stepwise N−I transitions, the magnetic susceptibility (χ), which has a typical value of 3.07×10^{-3} cm^3 mol^{-1} (χT = 0.921 cm^3 K mol^{-1}) at 300 K due to the nature of the isolated $[Ru_2^{II,II}]$ species,[37−39] exhibited anomalies at T_1 and T_2 and ultimately increased due to a ferrimagnetic arrangement of the generated spins with a decrease in T (Figure 6). No χ peak was observed down to 1.8 K even in applied fields of 3−1000 Oe (Figure S2, Supporting Information), and χT did not show a minimum. Nevertheless, the saturated magnetization ($M_s = 1.3\,\mu_B$) at 7 T in a M vs H plot at 1.8 K confirms that there is an intrachain ferrimagnetic arrangement (Figure 7 and Figure S3, Supporting Information),[55] indicating the presence of a strong 1-D correlation just below T_2. The M_s value, which is smaller than the expected value of 2 μ_B with $g = 2.0$, was attributed to strong magnetic anisotropy of $[Ru_2^{II,III}]^+$ unit, which has been observed in

dx.doi.org/10.1021/ja110007u |J. Am. Chem. Soc. 2011, 133, 5338–5345

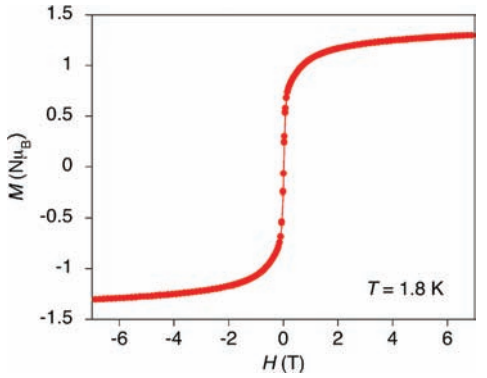

Figure 7. Field dependence of the magnetization at 1.8 K, where the saturation value of the magnetization is 1.3 μ_B at 7 T.

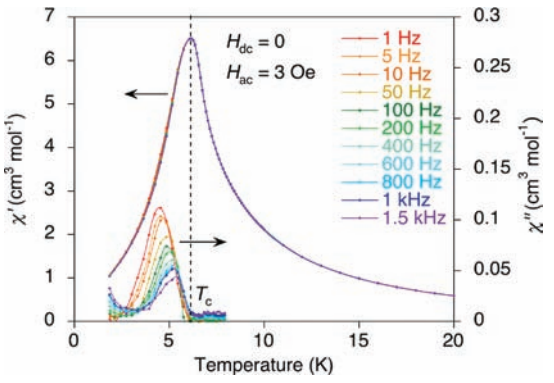

Figure 8. Temperature dependence of the ac susceptibilities (χ', in-phase; χ'', out-of-phase) measured at several ac frequencies in a 0 dc field and a 3 Oe oscillating field.

$[Ru_2]_2TCNQ$ systems[45−48] (zero-field splitting parameter $D \approx 60-70$ cm^{-1} in $[Ru_2^{II,III}]^+$ with $S = 3/2$[39,37]). Though the presence of large anisotropy in a 1-D system makes it difficult to evaluate accurately the magnitude of the intrachain exchange coupling, simulation of the χT vs T curve using an alternating chain model[56] with $S_i = 3/2$ and $S_{i+1} = 1/2$ in the Hamiltonian $H = -2J\Sigma_{i=1}^{N} \vec{s}_i \cdot \vec{s}_{i+1}$ afforded a large antiferromagnetic exchange parameter (J/k_B) of ca. −169 K with $g_{rad} = 2.0$ (fixed) and $g_{Ru} = 1.94$ in the T range of 50−190 K (solid red line in Figure 6). Furthermore, on the basis of the T dependence of the ac susceptibilities (Figure 8), 3-D ferrimagnetic ordering occurs somewhat viscously at 6.2 K due to the presence of interchain ferromagnetic interactions (Figure S2, Supporting Information for the temperature dependence of the field-cooled magnetization at several weak fields). Thus, the change in the magnetism sensitively occurs with the N−I phase transitions.

The variation in the N−I transitions as a function of hydrostatic pressure was investigated using a piston-cylinder-type cell made of Cu−Be alloy in a SQUID magnetometer.[57,58] Figure 9a shows temperature dependence of the magnetization under various applied pressures, and Figure 9b is a diagram of pressure versus T. T_1 and T_2 are dependent on the hydrostatic pressure. Even at low pressures less than 1 kbar, T_1 and T_2 sensitively shift to higher T at the same rate without overlapping up to 320 K. This result supports that the IM phase forms due to the interchain Coulomb interactions. The hydrostatic pressure isotropically affects the area between chains as well as within chains. In this situation, the Coulomb energy cost and gain, which are

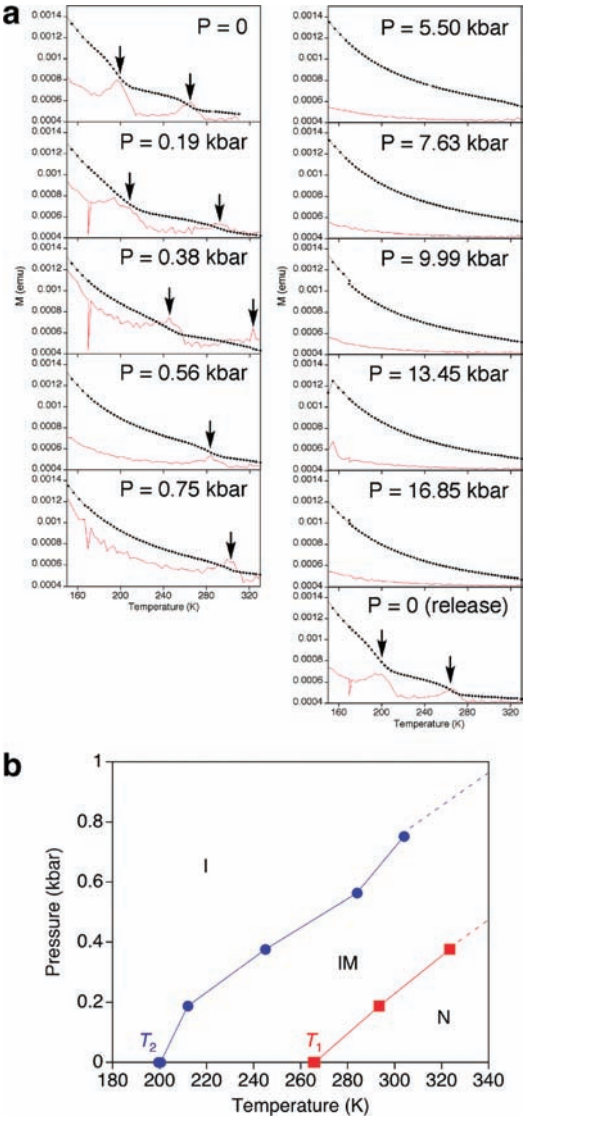

Figure 9. Pressure dependence of the N−I transitions. (a) Temperature dependence of the magnetization (M) under several hydrostatic pressures up to 16.85 kbar, where the red line represents a profile of dM/dT. After applying pressures, the pressure was released to the ambient pressure (see P = 0 (release)), at which the feature of the magnetization as well as the transition temperatures was completely recovered, indicating the reversibility of the magnetic behavior and the stability of the sample under an applied pressure. (b) A phase diagram of pressure versus T.

expected to be between chains along the c axis and in the ⟨011⟩ direction, respectively, increase at the same rate.

CONCLUDING REMARKS

The first example of a covalently bonded DA chain complex exhibiting the N−I transition was reported. In addition, the stepwise feature involving an IM phase, i.e., 'devil's staircase,' is the first demonstration in the temperature-induced N−I phase transition. The IM phase is comprised of a 1:1 mixture of N and I chains. From a full structural analysis, N and I chains alternate in the crystal due to anisotropic interchain Coulomb interactions. The most important aspect is the fact that Coulomb interactions as well as the relation between the ionization potential of D and

dx.doi.org/10.1021/ja110007u |J. Am. Chem. Soc. 2011, 133, 5338–5345

the electron affinity of A control the long-range charge distribution in the solid state of homogeneous species. This knowledge is not only important for understanding electronic materials but can also be used to obtain new dynamic functionalities via synergistic correlations among charge, spin, and lattice.

EXPERIMENTAL SECTION

Synthesis of 1. All synthetic procedures were performed under an inert atmosphere using standard Schlenk-line techniques and a commercial glovebox. A CH_2Cl_2 solution (10 mL) of DMDCNQI (4.6 mg, 0.025 mmol) was separated into 2 mL portions (bottom layer) and placed in narrow diameter sealed glass tubes (ϕ: 8 mm). A mixture of *p*-xylene and CH_2Cl_2 (1:1 v/v; 1 mL) was added. A *p*-xylene solution (10 mL) of $[Ru_2(2,3,5,6\text{-}F_4PhCO_2)_4(THF)_2]$ (26 mg, 0.025 mmol) was carefully placed in 2 mL portions into the middle layer, and slow diffusion was allowed to occur. The glass tubes were left undisturbed for one month or more to yield plate-shaped brown crystals of **1**. Elemental analysis (%) calcd for **1** $C_{54}H_{32}F_{16}N_4O_8Ru_2$: C, 47.31; H, 2.35; N, 4.09. Found: C, 47.34; H, 2.41; N, 4.08. IR (KBr measured on a JASCO FT-IR 620): ν(C≡N), 2109 cm^{-1}; ν(C═C), 1536 cm^{-1}; $\nu(CO_2)$, 1586, 1403 cm^{-1}.

Physical Measurements. Infrared (IR) absorption spectra were measured as KBr disks at room temperature on a JASCO FT-IR 620 spectrophotometer, and the temperature dependence of IR absorption spectra were measured on a single crystal in the temperature range of 200−300 K using a JASCO IRT-5000 infrared microscope with a He cryostat. DSC data were collected on a Shimadzu DSC-60 instrument in the temperature range of 275−150 K with a sweep rate of 5 °C/min. The temperature dependence of dc electrical resistivity on five single crystals from different batches with approximately dimensions of 100 × 50 × 40 μm was measured using an Agilent 34420A nanovoltmeter using a two-probe technique. The source voltage was fixed at 1 V. Electrical contacts to the crystal were made with 15 μm platinum wire and carbon paste. Magnetic susceptibility measurements were conducted on a SQUID magnetometer (Quantum Design MPMS-XL) in the temperature range of 1.8−300 K. AC measurements were performed at various frequencies ranging from 1 to 1488 Hz with an ac field amplitude of 3 Oe. Polycrystalline samples were embedded in liquid paraffin. The diamagnetic contributions of the sample holder and liquid paraffin were calculated from Pascal constants and subtracted from the raw data. Magnetic measurements under hydrostatic pressures up to 16.85 kbar were carried out using a piston-cylinder-type cell made of Cu−Be alloy in the SQUID magnetometer.[57] The sample was dispersed into Apiezon-J oil, which was used as a pressure-transmitting medium with a piece of Pb, whose superconducting transition temperature can be used as a probe to estimate the actual pressure. The mixture was placed in a Teflon bucket and fixed in a cell clamp.

Single-Crystal X-ray Crystallography at the Laboratory Level. Crystal data were collected on a CCD diffractometer (Rigaku Saturn VariMax) with graphite-monochromated Mo Kα radiation (λ = 0.71070 Å). A single crystal with dimensions of 0.21 × 0.12 × 0.02 mm was mounted on a thin-glass loop and cooled in an N_2 gas stream to a temperature in the range of 107−282 K (heating process). The absolute temperature was determined using a thermocouple located at the sample position. The structures were solved using direct methods (SIR97). The nonhydrogen atoms were refined anisotropically, and hydrogen atoms were introduced at fixed positions. Full-matrix least-squares refinements on F^2 converged with unweighted and weighted agreement factors of $R_1 = \Sigma||F_o| - |F_c||/\Sigma|F_o|$ ($I > 2.00\sigma(I)$ and all data), and $wR_2 = [\Sigma w(F_o^2 - F_c^2)^2/\Sigma w(F_o^2)^2]^{1/2}$ (all data). A Sheldrick weighting scheme was used. CCDC-793287 contains the data obtained at 107 K and the supplementary crystallographic data for **1**. These data can be obtained free of charge from The Cambridge Crystallographic Data Centre via www.ccdc.cam.ac.uk/data_request/cif. Crystal data for **1** at 107 K: $C_{54}H_{32}F_{16}N_4O_8Ru_2$, M_r = 1370.98, monoclinic, space group $P2_1/n$, a = 14.760(5) Å, b = 10.519(3) Å, c = 17.152(6) Å, β = 97.265(5)°, V = 2641.7(15) Å^3, Z = 2, λ = 0.71070 Å, μ = 6.878 cm^{-1}, D_{calc} = 1.723 g cm^{-3}, F_{000} = 1360.00, T = 107(1) K; 20 767 reflections, 5983 unique, R_{int} = 0.050; final refinement to convergence on F^2 gave R_1 = 0.0527 ($I > 2\sigma(I)$), R_1 = 0.0702 (all data) and wR_2 = 0.1195 (all data), goodness of fit (GOF) = 1.093. The data at other temperatures are summarized in Table S5, Supporting Information.

Single-Crystal X-ray Crystallography Using a Synchrotron Beam. X-ray diffraction measurements were performed using a cylindrical imaging plate detector installed in the beamline BL-8B at the Photon Factory, KEK, Japan. The incident X-ray beam was monochromatized to 0.6888 Å by using a Si (111) double-crystal monochromator. The wavelength was calibrated using a powder diffraction pattern of CeO_2. High-quality single crystals with typical dimensions of 0.12 × 0.07 × 0.02 mm^3 were used. The sample was mounted on a thin-glass loop and cooled by an N_2 gas stream. Data acquisition was performed at 180, 240, and 280 K. All nonhydrogen atoms were refined anisotropically using SHELXL, and hydrogen atoms were ignored. Results of the analysis for 180 and 280 K agree with those at laboratory level. Structure analysis for 240 K was performed by allowing the presence of twin. The volume fraction obtained by the least-squares fitting is consistent with the ratio in intensities of split peaks, as shown in Figure 3c. Crystal data at 240 K are as follows: Triclinic system, space group $P-1$, a = 14.803(2) Å, b = 21.2201(4) Å, c = 20.4174(9) Å, α = 121.201(2)°, β = 96.222(10)°, γ = 90.121(4)°, V = 5440.6(9) Å^3, Z = 4, 30 704 reflections, 14 713 unique, R_{int} = 0.0479; R_1 = 0.0381 ($I > 2\sigma(I)$), R_1 = 0.0663 (all data) and wR_2 = 0.1177 (all data), goodness of fit (GOF) = 0.870. Structural parameters, Ru−O distances, and bond lengths of DMDCNQI are listed in Tables S3 and S4, Supporting Information, respectively. CCDC-812097 contains the data at 240 K obtained in this technique. These data can be obtained free of charge from The Cambridge Crystallographic Data Centre.

ASSOCIATED CONTENT

Supporting Information. X-ray crystallographic file in CIF format for the measurement at 107 K for **1**, bond distances and unit cell parameters determined using the monoclinic space group $P2_1/n$ in the temperature range of 107−282 K, bond distances at 240 K in relation to the triclinic space group $P-1$ obtained using a synchrotron X-ray source, and additional figures. This material is available free of charge via the Internet at http://pubs.acs.org.

AUTHOR INFORMATION

Corresponding Author

miyasaka@agnus.chem.tohoku.ac.jp

*After April 1, 2011: Department of Chemistry, Division of Material Sciences, Graduate School of Natural Science and Technology, Kanazawa University, Kakuma, Kanazawa 920-1192, Japan. E-mail: miyasaka@se.kanazawa-u.ac.jp. Telephone: +81-76-264-5697.

ACKNOWLEDGMENT

The authors thank S. Takaishi (Tohoku University) for helping with resistivity and IR measurements, A. Nakao (Institute of Materials Structure Science, KEK) for helping with crystal structure analysis at Photon Factory, M. Nakano (Osaka University) for simulations and discussions on $M-H$ curves in several models, B. K. Breedlove (Tohoku University) for helpful discussions on preparing the manuscript, and K. R. Dunbar (Texas A&M University) for helpful discussion on the work. H. M. is thankful for financial support from a Grant-in-Aid for Scientific Research from the Ministry of Education, Culture,

Sports, Science, and Technology, Japan (grant no. 21350032) and The Asahi Glass Foundation.

REFERENCES

(1) Batail, P. *Chem. Rev.* **2004**, *104*, 4887−5782.
(2) Saito, G.; Yoshida, Y. *Bull. Chem. Soc. Jpn.* **2007**, *80*, 1–137.
(3) Torrance, J. B.; Vazquez, J. E.; Mayerle, J. J.; Lee, V. Y. *Phys. Rev. Lett.* **1981**, *46*, 253–257.
(4) Torrance, J. B.; Girlando, A.; Mayerle, J. J.; Crowley, J. I.; Lee, V. Y.; Batail, P. *Phys. Rev. Lett.* **1981**, *47*, 1747–1750.
(5) Tokura, Y.; Okamoto, H.; Koda, T.; Mitani, T.; Saito, G. *Solid State Commun.* **1986**, *57*, 607–610.
(6) Mitani, T.; Kaneko, Y.; Tanuma, S.; Tokura, Y.; Koda, T.; Saito, G. *Phys. Rev. B* **1987**, *35*, 427–429.
(7) Kaneko, Y.; Tanuma, S.; Tokura, Y.; Koda, T.; Mitani, T.; Saito, G. *Phys. Rev. B* **1987**, *35*, 8024–8029.
(8) Hasegawa, T.; Akutagawa, T.; Nakamura, T.; Mochida, T.; Kondo, R.; Kagoshima, S.; Iwasa, Y. *Phys. Rev. B* **2001**, *64*, 085106−1−7.
(9) Basaki, S.; Matsuzaki, S. *Solid State Commun.* **1994**, *91*, 865–868.
(10) Farina, L.; Brillante, A.; Masino, M.; Girlando, A. *Phys. Rev. B* **2001**, *64*, 144102−1–6.
(11) Iwasa, Y.; Watanabe, N.; Koda, T.; Saito, G. *Phys. Rev. B* **1993**, *47*, 2920–2923.
(12) Sadogara, R.; Matsuzaki, S. *Mol. Cryst. Liq. Cryst.* **1997**, *296*, 269–280.
(13) Koshihara, S.; Tokura, Y.; Mitani, T.; Saito, G.; Koda, T. *Phys. Rev. B* **1990**, *42*, 6853–6856.
(14) Koshihara, S.; Takahashi, Y.; Sakai, H.; Tokura, Y.; Luty, T. *J. Phys. Chem. B* **1999**, *103*, 2592–2600.
(15) Luty, T.; Cailleau, H.; Koshihara, S.; Collet, E.; Takesada, M.; Lemée-Cailleau, M. H.; Buron-Le Cointe, M.; Nagaosa, N.; Tokura, Y.; Zienkiewicz, E.; Ouladdiaf, B. *Europhys. Lett.* **2002**, *59*, 619–625.
(16) Collet, E.; Lemée-Cailleau, M.−H.; Buron-Le Cointe, M.; Cailleau, H.; Wulff, M.; Luty, T.; Koshihara, S.; Meyer, M.; Toupet, L.; Rabiller, P.; Techert, S. *Science* **2003**, *300*, 612–615.
(17) Okamoto, H.; Ishige, Y.; Tanaka, S.; Kishida, H.; Iwai, S.; Tokura, Y. *Phys. Rev. B* **2004**, *70*, 165202−1–18.
(18) Mitani, T.; Saito, G.; Tokura, Y.; Koda, T. *Phys. Rev. Lett.* **1984**, *53*, 842–845.
(19) Okamoto, H.; Mitani, T.; Tokura, Y.; Koshihara, S.; Komatsu, T.; Iwasa, Y.; Koda, T.; Saito, G. *Phys. Rev. B* **1991**, *43*, 8224–8232.
(20) Horiuchi, S.; Kumai, R.; Okimoto, Y.; Tokura, Y. *Chem. Phys.* **2006**, *325*, 7–91.
(21) Horiuchi, S.; Okimoto, Y.; Kumai, R.; Tokura, Y. *J. Am. Chem. Soc.* **2001**, *123*, 665–670.
(22) Horiuchi, S.; Tokura, Y. *Nat. Mater.* **2008**, *7*, 357–366.
(23) Kagawa, F.; Horiuchi, S.; Tokunaga, M.; Fujioka, J.; Tokura, Y. *Nat. Phys.* **2010**, *6*, 169–172.
(24) Iwasa, Y.; Koda, T.; Koshihara, S.; Tokura, Y.; Iwasawa, N.; Saito, G. *Phys. Rev. B* **1989**, *39*, 10441–10444.
(25) Tokura, Y.; Okamoto, H.; Koda, T.; Mitani, T.; Saito, G. *Phys. Rev. B* **1988**, *38*, 2215–2218.
(26) Horiuchi, S.; Kumai, R.; Okimoto, Y.; Tokura, Y. *Synth. Met.* **2003**, *133*−*134*, 615–618.
(27) Horiuchi, S.; Okimoto, Y.; Kumai, R.; Tokura, Y. *J. Phys. Soc. Jpn.* **2000**, *69*, 1302–1305.
(28) Aoki, S.; Nakayama, T.; Miura, A. *Phys. Rev. B* **1993**, *48*, 626–629.
(29) Aoki, S.; Nakayama, T.; Miura, A. *Synth. Met.* **1995**, *70*, 1243–1244.
(30) Iwasa, Y.; Koda, T.; Tokura, Y.; Kobayashi, A.; Iwasawa, N.; Saito, G. *Phys. Rev. B* **1990**, *42*, 2374–2377.
(31) Aoki, S.; Nakayama, T. *Phys. Rev. B* **1997**, *56*, R2893–R2896.
(32) Lemée-Cailleau, M. H.; Buron-Le Cointe, M.; Cailleau, H.; Luty, T.; Moussa, F.; Roos, J.; Brinkmann, D.; Toudic, B.; Ayache, C.; Karl, N. *Phys. Rev. Lett.* **1997**, *79*, 1690–1693.
(33) Le Cointe, M.; Lemée-Cailleau, M. H.; Cailleau, H.; Toudic, B.; Toupet, L.; Heger, G.; Moussa, F.; Schweiss, P.; Kraft, K. H.; Karl, N. *Phys. Rev. B* **1995**, *51*, 3374–3386.
(34) Hubbard, J.; Torrance, J. B. *Phys. Rev. Lett.* **1981**, *47*, 1750–1754.
(35) Bak, P. *Rep. Prog. Phys.* **1982**, *45*, 587–629.
(36) Bruinsma, R.; Bak, P.; Torrance, J. B. *Phys. Rev. B* **1983**, *27*, 456–466.
(37) Miyasaka, H.; Clérac, R.; Campos-Fernández, C. S.; Dunbar, K. R. *J. Chem. Soc., Dalton Trans.* **2001**, 858–861.
(38) Aquino, M. A. S. *Coord. Chem. Rev.* **1998**, *170*, 141–202.
(39) Cotton, F. A.; Walton, R. A. *Multiple Bonds Between Metal Atoms*, 2nd ed.; Oxford University Press: Oxford, England, 1993.
(40) Mikuriya, M.; Yoshioka, D.; Handa, M. *Coord. Chem. Rev.* **2006**, *250*, 2194–2211.
(41) Aumüller, A.; Hünig, S. *Angew. Chem., Int. Ed. Engl.* **1984**, *23*, 447–448.
(42) Hünig, S.; Kemmer, M.; Meixner, H.; Sinzger, K.; Wenner, H.; Bauer, T.; Tillmanns, E.; Rudolf Lux, F.; Hollstein, M.; Gross, H.−G.; Langohr, U.; Werner, H.−P.; von Schütz, J. U.; Wolf, H.−C. *Eur. J. Inorg. Chem.* **1999**, 899–916.
(43) Hünig, S.; Herberth, E. *Chem. Rev.* **2004**, *104*, 5535–5563.
(44) Miyasaka, H.; Campos-Fernández, C. S.; Clérac, R.; Dunbar, K. R. *Angew. Chem., Int. Ed.* **2000**, *39*, 3831–3835.
(45) Miyasaka, H.; Izawa, T.; Takahashi, N.; Yamashita, M.; Dunbar, K. R. *J. Am. Chem. Soc.* **2006**, *128*, 11358–11359.
(46) Motokawa, N.; Miyasaka, H.; Yamashita, M.; Dunbar, K. R. *Angew. Chem., Int. Ed.* **2008**, *47*, 7760–7763.
(47) Motokawa, N.; Oyama, T.; Matsunaga, S.; Miyasaka, H.; Yamashita, M.; Dunbar, K. R. *CrystEngComm* **2009**, *11*, 2121–2130.
(48) Miyasaka, H.; Motokawa, N.; Matsunaga, S.; Yamashita, M.; Sugimoto, K.; Mori, T.; Toyota, N.; Dunbar, K. R. *J. Am. Chem. Soc.* **2010**, *132*, 1532–1544.
(49) Miyasaka, H.; Morita, T.; Yamashita, M. *Chem. Commun.* **2011**, *47*, 271–273.
(50) Miyasaka, H.; Motokawa, N.; Atsuumi, R.; Kamo, H.; Asai, Y.; Yamashita, M. *Dalton Trans.* **2011**, *40*, 673–682.
(51) Kistenmacher, T. J.; Emge, T. J.; Bloch, A. N.; Cowan, D. O. *Acta Cryst., Sect. B* **1982**, *38*, 1193–1199.
(52) Miyasaka, H.; Campos-Fernández, C. S.; Galán-Mascarós, J. R.; Dunbar, K. R. *Inorg. Chem.* **2000**, *39*, 5870–5873.
(53) Sugiura, K.; Mikami, S.; Johnson, M. T.; Raebiger, J. W.; Miller, J. S.; Iwasaki, K.; Okada, Y.; Hino, S.; Sakata, Y. *J. Mater. Chem.* **2001**, *11*, 2152–2158.
(54) Okamoto, H.; Komatsu, T.; Iwasa, Y.; Koda, T.; Tokura, Y.; Koshihara, S.; Mitani, T.; Saito, G. *Synth. Met.* **1988**, *27*, B189–B196.
(55) The $M-H$ curve for a model of a square ring composed of S_i = 3/2 and s_{i+1} = 1/2 regarding fixed parameters of g_{rad} = 2.0 and g_{Ru} = 2.2, respectively, was simulated as respective variable parameters of D for S_i = 3/2 and J; See Figure S3, Supporting Information. These results indicate that the ferrimagnetic spin arrangement is justifiable for **1**.
(56) Drillon, M; Coronado, E.; Beltran, D.; Georges, R. *Chem. Phys.* **1983**, *79*, 449–453.
(57) Mito, M. *J. Phys. Soc. Jpn. Suppl. A* **2007**, *76*, 182–185.
(58) Motokawa, N.; Miyasaka, H.; Yamashita, M. *Dalton Trans.* **2010**, *39*, 4724–4726.